文章编号：1001-9014(XXXX)XX-0001-11

DOI:10.11972/j.issn.1001-9014.XXXX.XX.001

Mid-wavelength infrared detector array based on black phosphorus ink thin film

ZHU Long-Hai[1], DUAN Shi-Kun[2], CHEN Mao-Hua[2], BAI Yu-Zhuo[2], ZHAO Tian-Ge[2], YU Yi-Ye[2], WEI Qin[3], XU Teng-Fei[3], WANG Zhen[2*], HU Wei-Da[1,2*]

(1. School of Microelectronics, Shanghai University, Shanghai 201800, China;
2. State Key Laboratory of Infrared Science and Technology, Shanghai Institute of Technical Physics, Chinese Academy of Sciences, Shanghai 200083, China;
3. School of Microelectronics and School of Integrated Circuits, Nantong University, Nantong 226019, China)

Abstract: Mid-wavelength infrared (MWIR) imaging technology plays a crucial role in aerospace, medical diagnostics, and autonomous driving. Van der Waals material black phosphorus (BP) exhibits exceptionally high carrier mobility and an ideal direct bandgap, making it a proven candidate for high-performance room-temperature MWIR sensing. However, the stringent growth conditions and anisotropic growth characteristics restrict the development of BP optoelectronic devices to small-scale laboratory demonstrations. Therefore, there is an urgent need to develop large-scale, uniform, and high-performance BP photodetector arrays. This study employed a room temperature preparation technique to deposit a large-area, uniform, low-oxidation BP ink film onto thin-film transistors, resulting in the development of a 64 × 64 high-performance MWIR snapshot photodetector array. The room temperature ink preparation process effectively prevents the oxidation of BP during fabrication, achieving an oxidation loss as low as 1.12%. In addition, a gradient centrifugation strategy was employed to optimize the lateral size and thickness distribution of the nanosheets in the BP ink, thereby facilitating the transport of charge carriers. The BP ink film array demonstrated a high photoresponsivity of 4.52 mA/W in the MWIR range, with pixel light response non-uniformity as low as 10.1%. This study presents a new approach for advancing large-scale MWIR imaging technology.

Key words: black phosphorus, ink film, mid-wavelength infrared, snapshot imaging

基于黑磷油墨薄膜的中波红外探测器阵列

朱龙海[1], 段世坤[2], 陈茂华[2], 白雨卓[2], 赵天歌[2], 余羿叶[2], 卫 钦[3], 徐腾飞[3], 王 振[2*], 胡伟达[1,2*]

(1. 上海大学 微电子学院,上海 201800;
2. 中国科学院上海技术物理研究所 红外科学与技术全国重点实验室,上海 200083;
3. 南通大学 微电子学院(集成电路学院),江苏 南通 226019)

摘要:中波红外成像技术在航空航天、医疗诊断和自动驾驶等领域发挥着至关重要的作用。范德华材料黑磷凭借其极高的载流子迁移率和理想的直接带隙,已被证实是构建高性能室温中波红外传感器的有力候选材料。然而,严苛的生长条件及各向异性的生长特性,限制了黑磷光电器件的发展,目前仍停留在小规模实验

Received date: 2026-02-02, **revised date**: 2026-02-24 **收稿日期**:2026-02-02,**修回日期**:2026-02-24

Foundation items: Supported by the National Key Research and Development Program of China (2023YFB3611400, 2025YFF0524500), National Natural Science Foundation of China (62475275, 62174063, 62174061, U24A20295, 62404230, 62504231 to H. X.), China Postdoctoral Science Foundation (2023TQ0362, GZB20230795, 2024M753366), Basic and Applied Basic Research Foundation of Guangdong Province (2023B1515120049), and the Natural Science Foundation of Shanghai (25ZR1402544 to H. X.), and the National Science Centre (NCN) and the National Natural Science Foundation of China (NSFC) "SHENG 3" UMO-2023/48/Q/ST7/0014 (NCN) and 162361136587 (NSFC)

Biographies: ZHU Long-Hai (2000-), male, Nantong, a master's student. Research area involves two-dimensional materials and their inks. E-mail: zlh3218910@163.com; Duan Shi-Kun (1998-), male, Yantai, a PhD student. Research area involves optics and microstructures. E-mail: d15524893168@163.com.

* **Corresponding authors**: E-mail: wangzhen@mail.sitp.ac.cn; wdhu@mail.sitp.ac.cn

室演示阶段。因此,开发大规模、均匀且高性能的黑磷光电探测器阵列迫在眉睫。本研究采用室温制备技术,将大面积、均匀、低氧化的黑磷油墨薄膜沉积到薄膜晶体管上,成功研制出64×64的高性能中波红外快照式光电探测器阵列。该室温油墨制备工艺有效防止了黑磷在加工过程中的氧化,实现了低至1.12%的氧化损耗率。此外,通过梯度离心策略优化了黑磷油墨中纳米片的粒径与厚度分布,从而促进了电荷载流子的传输。该黑磷油墨薄膜阵列在中波红外波段展现出4.52 mA/W的高光响应度,像素光响应非均匀性低至10.1%。本研究为推进大规模中波红外成像技术的发展提供了一条新路径。

关 键 词:黑磷;油墨薄膜;中波红外;快照成像

中图分类号:O43 **文献标识码**:A

Introduction

Mid-wavelength infrared (MWIR) imaging is a technique for image acquisition and analysis in the MWIR band (3 - 5 μm)[1-5]. As the primary atmospheric window for infrared radiation, MWIR imaging exhibits low sensitivity to the atmosphere, enabling better capture of the infrared radiation characteristics of various substances[6-8]. This technique has demonstrated significant potential in medical diagnostics[9, 10], environmental monitoring[11, 12], industrial applications[13, 14], and aerospace [15, 16]. The core components of imaging cameras are MWIR photodetector arrays, typically constructed from narrow bandgap semiconductor materials such as InSb[17, 18], HgCdTe[19-22], and type-II superlattices[23, 24]. Although these technologies have been established for decades, they have long struggled to overcome challenges related to epitaxial growth constrained by lattice matching[25, 26] and excessive thermal noise at room temperature[27].

Two-dimensional van der Waals (vdW) narrow bandgap material black phosphorus (BP) has emerged as a promising candidate for MWIR photodetector applications[28, 29]. BP thin films, produced through mechanical exfoliation, have shown effective performance in unit photodetectors, achieving high sensitivity MWIR detection at room temperature[30, 31]. However, the stringent growth conditions and anisotropic growth characteristics restrict the development of BP optoelectronic devices to small-scale laboratory demonstrations[32]. Consequently, these small-scale array devices can only collect imaging data via a step-scanning module during the imaging process, which falls short of achieving MWIR snapshot imaging.

Liquid-phase exfoliation technology, in conjunction with solution treatment, offers a scalable alternative for fabricating infrared photodetector arrays[33, 34]. By formulating BP crystals into an ink, thin films at the centimeter scale can be produced, allowing for concept validation of single-pixel MWIR detection when biased[35]. More importantly, vdW interface of this BP ink-based film is not limited by lattice matching, making it compatible with commercial CMOS processes for large-scale production. However, BP ink films impose strict requirements on particle size and thickness. Larger BP nanosheets can create pinhole structures within the thin film, undermining array uniformity; conversely, BP nanosheets that are excessively small may exhibit a bandgap exceeding 0.33 eV, which hampers mid-infrared light absorption[36]. Furthermore, as a material prone to oxidation, the elevated processing temperatures associated with liquid-phase exfoliation can exacerbate the oxidation of small BP particles, thereby degrading the performance of the film detectors[37]. The existing BP ink preparation process is limited by the overlap and aggregation between BP layers, making it difficult to obtain a single component with a truly narrow particle size distribution. This has kept the response uniformity and responsivity of the BP ink film detector array at a bottleneck. Thus, the preparation of BP ink with controlled particle size and thickness distribution, along with the fabrication of large-scale, uniform, and stable BP thin film infrared photodetector arrays, remains a critical challenge.

Here, we developed a MWIR imaging array by integrating BP ink films with silicon-based thin-film transistors, successfully demonstrating mid-infrared imaging at room temperature. To enhance pixel uniformity across a large scale, we employed a gradient centrifugation strategy to prepare BP nanosheets with concentrated particle size and thickness distributions, resulting in dark current non-uniformity as low as 10.16% and response non-uniformity of 10.1%. Utilizing low boiling point ethanol as a dispersant, the entire process of ink film preparation was conducted at a temperature as low as 78.3 °C, significantly mitigating performance degradation caused by the spontaneous oxidation of BP nanosheets. The BP thin film array achieved a response rate of 4.8 $mA \cdot W^{-1}$ in the wavelength range of 0.6-4 μm, with a response time of 206 μs. Based on this high-quality BP thin film array, we developed a 64 × 64 single-shot camera capable of demonstrating letter pixel imaging under 3.3 μm wavelength radiation at an imaging frame rate of 10.9 fps. This high-quality thin film detector represents a significant advancement toward realizing the next generation of room temperature, high-performance, and CMOS-compatible mid-infrared optoelectronic imaging technology.

1 Experimental Section

1.1 Ink Preparation and Spin-Coating Process

A schematic illustration of the BP ink preparation process is shown in Figure S1. Bulk BP crystals were first ground into sub-millimeter powders using either a mortar and pestle or a ball mill. Approximately 15 – 20 mg of the BP powder was added into a 10 mL beaker containing 1.5 mL of anhydrous N-methyl-2-pyrrolidone (NMP). The mixture was then sonicated using a probe-type ultrasonic processor with a maximum power of 150

W. To suppress overheating during sonication, the output power was set to 50% of the maximum, with a 50% duty cycle. The sonication time was varied from 20 to 180 min to control the thickness and lateral size of the BP flakes. After sonication, the dispersion was transferred into 5 mL centrifuge tubes, and a stepwise centrifugation process was performed to select BP flakes of suitable size. In the first step, the dispersion was centrifuged at 2000 rpm for 30 min to remove large BP particles, and the supernatant was transferred to a new centrifuge tube. In the second step, the supernatant was centrifuged at 8000 rpm for 30 min; the top layer containing small particles was discarded, and the black precipitate at the bottom was retained. A small amount of NMP was intentionally left in the tube to improve the solubility of BP in the final dispersion. Next, 0.2 mL of anhydrous ethanol and 25 μL of oleylamine were added to the retained BP sediment, followed by a 2 min ultrasonic treatment in a water bath to ensure uniform dispersion. Oleylamine was introduced to enhance the stability of BP flakes in solution. The dispersion was then centrifuged again at 8 000 rpm for 30 min, and the supernatant was discarded. Finally, 0.2 mL of anhydrous ethanol was added, followed by another 2 min ultrasonic treatment in a water bath, yielding the final BP ink. Notably, anhydrous ethanol was chosen not only because of its lower boiling point compared to NMP, which facilitates subsequent spin-coating, but also due to its ability to dissolve oleylamine effectively. To prepare BP thin films, the as-prepared ink was spin-coated onto SiO_2/Si or sapphire substrates at 200 rpm for 5 s followed by 1 200 rpm for 30 s. The coated films were then dried at room temperature for 1 – 2 min. Both the ink preparation and spin-coating processes were carried out entirely inside a nitrogen-filled glovebox to prevent oxidation of the black phosphorus.

1.2 Characterization of BP Ink and Films

The morphology and thickness of BP flakes were characterized using scanning electron microscopy (SEM, ZEISS GeminiSEM 300, Germany) and atomic force microscopy (AFM, Bruker Dimension Icon). To prevent aggregation of BP flakes that could affect statistical accuracy, the dispersions were further diluted with additional solvent before measurement. The same dilution strategy was applied during UV – Vis – NIR absorption spectroscopy to avoid signal saturation in the BP ink measurements. The molecular composition and crystal structure of the BP thin films were characterized using X-ray photoelectron spectroscopy (XPS, Thermo Scientific K-Alpha) and X-ray diffraction (XRD, Rigaku Smartlab 9 kW), respectively. The infrared absorption spectra of BP films were obtained in reflection – transmission mode using a Fourier-transform infrared (FTIR) spectrometer (Rigaku Smartlab 9 kW). Raman spectra and map were collected using a Raman spectrometer (HORIBA LabRAM HR Evolution) equipped with a 532 nm excitation laser.

1.3 Fabrication of Device and Array

The electrodes of the BP photodetector (Cr: 15 nm, Au: 45 nm) were deposited by dual ion beam sputtering through a fixed shadow mask directly onto the BP thin film. This method allows for precise control of electrode thickness while avoiding photoresist-induced degradation of the BP layer. The 64 × 64 TFT sensor chip (Linkzill) consisted of three functional regions: the common electrode area, the pixel area, and the pin area. The top surfaces of all three regions were composed of exposed indium tin oxide (ITO). The pixel area was silicon-based with a total size of 32 × 32 mm^2, and each pixel measured 500 μm × 500 μm. The BP photodetector array was fabricated by spin-coating BP ink onto the pixel region of the TFT backplane. Prior to spin-coating, the common electrode and pin regions were covered with PI tape to prevent contamination. The BP ink was spin-coated onto the bottom ITO electrodes and dried at room temperature. Afterward, the PI tape covering the common electrode region was removed, and a 15 nm Cr / 45 nm Au top electrode was deposited by dual ion beam sputtering. Finally, the tape on the pin region was removed, and the TFT chip was thermally pressed to connect it to the readout circuit for testing. Upon infrared illumination, the storage capacitors collected photo-generated holes driven by an external bias, and digital image signals were produced through an analog-to-digital converter (ADC). The acquired signals from the array sensor were transmitted to a mobile terminal via a wireless Wi-Fi module. The maximum frame rate of the readout system reached 10.9 fps.

1.4 Photoelectrical Performance Measurement

Lasers with wavelengths ranging from 633 to 1550 nm were provided by laser diodes (Thorlabs), with their output power controlled by a laser controller (Thorlabs ITC4001) and calibrated using an optical power meter (Thorlabs PM100D). For wavelengths beyond 2 μm, a tunable plasma laser (DSL-Laser) was employed as the illumination source, and its power was similarly calibrated using the same optical power meter. The response time was characterized using two types of oscilloscopes: an oscilloscope (Tektronix MDO3014) and a current preamplifier (SRS, Model SR570) connected to the measurement circuit. All the measurements of the BP devices and arrays were carried out at room temperature.

2 Results and Discussion

2.1 Preparation of BP ink guided by gradient centrifugation strategy

High-quality BP ink films are a prerequisite for achieving a mid-wavelength photodetector array. **Fig. 1 (a)** illustrates a simplified procedure for ink preparation and film formation. Commercial BP crystals are initially mechanically ground into sub-millimeter-sized powders. Subsequently, these BP powders are dispersed in N-methyl-2-pyrrolidone (NMP) and subjected to ultrasonic treatment to further reduce their particle size. It is important to note that water and oxygen barriers are required during the crushing and ultrasonic treatment processes to prevent the oxidation of BP powder. Oversized BP particles can lead to uneven film distribution, adversely affecting the effective transport of charge carriers. The gra-

dient centrifugation strategy has proven effective in screening the particle size of granular materials[38]. This strategy can eliminate larger particles at low speeds and smaller particles at high speeds, thereby retaining a relatively uniform size and thickness of the thin film, which is essential for ensuring the quality of the ink. Refer to Fig. S1 for more information on BP ink preparation process.

The BP dispersions at different centrifugal speeds (2, 4, 6, and 8 000 rpm) are depicted in Fig. S2. At higher centrifugal speeds, the increased settling force reduces the concentration of dispersed flakes, resulting in a more colorless supernatant. Correspondingly, as the centrifugation speed increases, the absorption intensity gradually decreases, indicating a sustained reduction in BP concentration within the dispersion. Typically, NMP is selected as a solvent and dispersant, providing higher stripping efficiency and better dispersion stability for BP ink preparation compared to other organic solvents[39]. Since BP is an easily oxidizable material, its oxidation is significantly influenced by temperature, necessitating the minimization of temperature during the ink preparation process[40]. Therefore, ethanol, which has a lower boiling point, was utilized as the solvent in this experiment, as its boiling point (78.3 °C) is lower than that of NMP (204 °C). Additionally, low-boiling-point ethanol effectively reduces the viscosity of the ink, enhancing its fluidity during use. In centrifugal operations, this aids in the dispersion and uniform distribution of BP particles. Furthermore, oleylamine was introduced as a binder, and mild ultrasonic treatment was applied to produce stable and uniform BP ink. The addition of oleylamine not only enhances the stability of BP flakes in the solution but also adjusts the viscosity and surface tension of the ink, facilitating the formation of a more uniform film during the subsequent spin coating process[41]. For more information on ink formulations and spin coating procedures, please refer to Method.

Table S1 summarizes the processing parameters under different ultrasonic treatment times and centrifugation conditions. The ultrasonic treatment times ranged from 20 to 180 minutes, progressively increasing from sample BP-A to sample D. Gradient control experiments were performed to further elucidate the centrifugation conditions for the samples. Sample A was prepared by centrifuging at 8 000 rpm for 30 minutes to remove sediment. In contrast, samples BP-B, C, and D underwent a two-step centrifugation process: centrifugation at 2 000 rpm for 30 minutes, followed by centrifugation at 8 000 rpm for 30 minutes. The morphological characterization and direct statistical analysis of the thickness and lateral dimensions of BP nanosheets were conducted using atomic force microscopy (AFM) and scanning electron microscopy (SEM), as depicted in Fig. 1(b) and Fig. 1(e). Notably, to visually capture the particle size of BP ink, the sample used for photography was diluted at a ratio of 1:5. The direct statistical analysis of the thickness and lateral dimensions of BP nanosheets is presented in the statistical histograms of Fig. 1(c) and Fig. 1(f). From the bottom panel of Fig. 1c, it is evident that due to the short ultrasonic treatment time and single-step centrifugation of sample BP-A, its lateral size distribution is broad, with a relatively large average size (~407.5 nm). As ultrasonic treatment time increases and two-step centrifugation is applied, the lateral size of the thin film decreases, resulting in a more uniform size distribution. Distribution of thickness shown in Fig. 1(f) exhibits a similar trend. Figures 1(d) and Fig. 1(g) display the thickness and average lateral size of BP slices. This confirms the effectiveness of the low-temperature gradient centrifugation strategy in preparing BP ink with controllable particle size.

2.2 Characterization of large-area BP ink film

BP has long been a subject of controversy due to its susceptibility to oxidation. To demonstrate the minimal effect of the gradient centrifugation strategy on BP, we performed X-ray photoelectron spectroscopy (XPS). The BP film was fabricated by spin coating BP ink onto a silicon substrate within a nitrogen-filled glovebox. **Figure 2 (a)** presents the XPS spectrum of the P 2p core energy level for the BP ink film. The spectrum displays a spin-orbit splitting doublet at 129.7 eV ($2p_{3/2}$) and 130.5 eV ($2p_{1/2}$), a signature feature of crystalline BP. Additionally, a broad peak centered at 134.5 eV is attributed to phosphorus oxide (P_xO_y), which typically exhibits emission peaks within the range of 132 - 136 eV[42]. The state of P_xO_y generation significantly influences the performance of BP optoelectronic devices. Figure S3 shows the XPS spectra under different processing methods. It is noteworthy that the BP ink prepared via spin coating, under conditions involving low boiling point solvents and oxygen barriers, exhibits extremely low oxidation loss, thereby ensuring the performance of subsequent optoelectronic devices. The comparison of common BP ink film preparation processes is shown in Table S2.

X-ray diffraction (XRD) presented in Fig. 2(b) illustrates the crystal structure of high-purity BP powder and BP ink film, indicating that the lattice orientation of the BP ink film aligns with that of the powder[43]. The consistency of the relative peak positions further suggests that the ink preparation process has minimal destructive impact on the BP materials. XRD analysis image of BP nanosheets dispersed using low boiling point process solvent is shown in Fig. S4. We measured the average reflection and transmission spectra of the BP ink film and subsequently calculated the absorption spectra, as depicted in Fig. 2(c). The transmission spectrum of BP film is shown in Fig. S5. The BP ink film exhibits characteristic infrared absorption extending into the MWIR region. The film's thickness distribution leads to variations in the bandgap across different areas, rendering it unreliable to extract the optical bandgap from the Tauc diagram, which accounts for the observed distribution in the absorption spectrum[44].

The Raman spectroscopy results presented in Fig. 2(d) demonstrate that the crystal structure of BP in the ink remains intact, matching with that of bulk BP. Characteristic peaks corresponding to the A_{1g}, B_{2g}, and A_{2g}

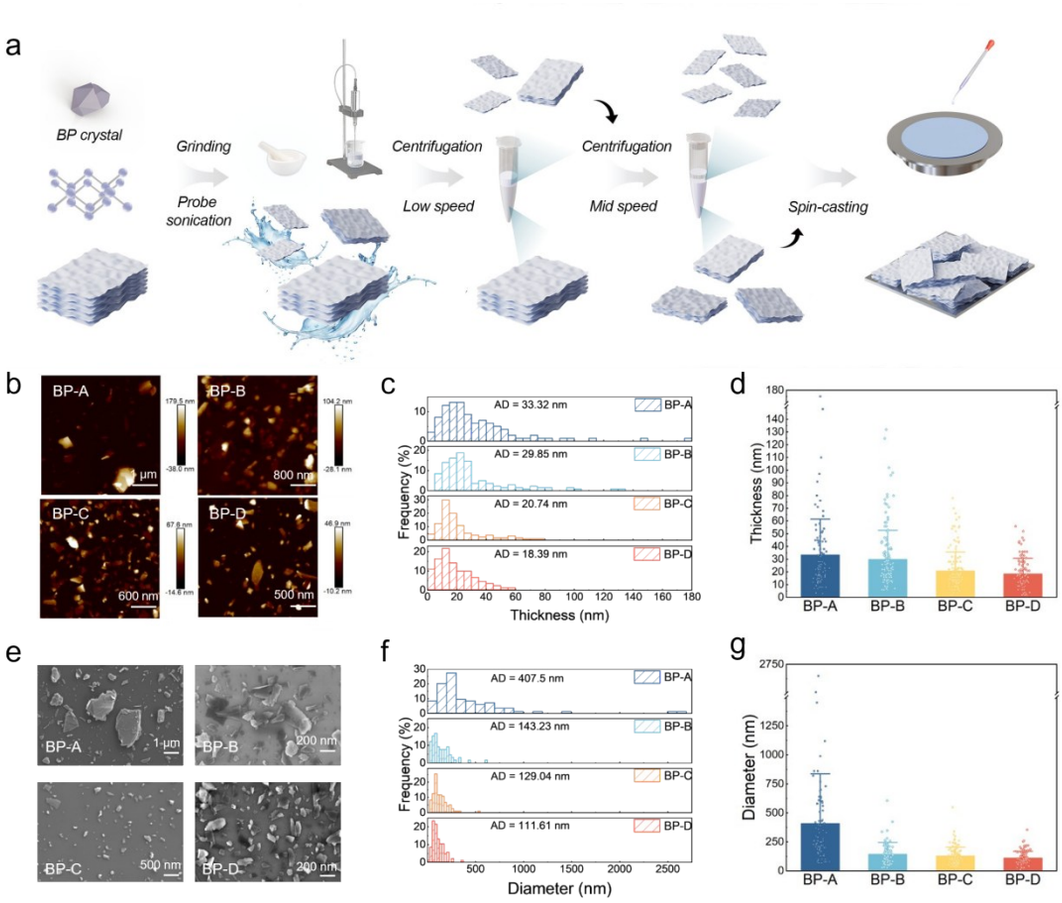

Fig. 1　Preparation process of BP ink with particle size concentration distribution guided by gradient centrifugation strategy: (a) Preparation process of BP ink and deposition techniques of BP ink; (b) Representative atomic force microscopic (AFM) images of solvent-exfoliated BP nanosheets under different grinding times and centrifugation conditions; (c) Histograms of thickness of BP nanosheets for different ink processing conditions from AFM images; (d) Bar - scatter plots of BP nanosheet, including thickness distribution and standard deviation; (e) SEM images of solvent-exfoliated BP nanosheets under different grinding times and centrifugation conditions; (f) Histograms of the lateral size of BP nanosheets for different ink processing conditions from SEM images; (g) Bar - scatter plots of BP nanosheet, including diameter distribution and standard deviation

图1　基于梯度离心策略引导的、具有粒径浓度分布的黑磷油墨制备过程:(a) 黑磷油墨的制备过程及沉积技术示意图;(b) 在不同研磨时间和离心条件下,溶剂剥离法制备的黑磷纳米片的代表性原子力显微镜图像;(c) 根据原子力显微镜图像统计的不同油墨处理条件下黑磷纳米片的厚度分布直方图;(d) 黑磷纳米片的条形-散点图,展示了厚度分布及标准偏差;(e) 在不同研磨时间和离心条件下,溶剂剥离法制备的黑磷纳米片的扫描电子显微镜图像;(f) 根据扫描电子显微镜图像统计的不同油墨处理条件下黑磷纳米片的横向尺寸分布直方图;(g) 黑磷纳米片的条形-散点图,展示了直径分布及标准偏差

phonon modes were observed at 361.9 cm^{-1}, 439.3 cm^{-1}, and 466.8 cm^{-1}, respectively[45, 46]. Since these peaks arise from the lattice vibrations of BP, their consistency confirms that the exfoliated BP flakes exhibit high crystallinity. To assess the low oxidation characteristics and uniformity of the ink films on a large scale, we conducted Raman mapping scans on BP ink films over an area of 100 × 100 μm^2, as illustrated in Fig. 2(e). The intensity in the mapping is defined as the ratio of A_{1g} to A_{2g} phonon intensity, which serves to directly illustrate the degradation of BP due to oxidation[47]. Typically, a higher ratio indicates a more severe oxidation effect on BP. The large-scale low ratio results suggest that the ink film is a pinhole-free film with uniform crystallinity at the sub-millimeter scale and has not been excessively oxidized during the preparation process. The statistical histogram in Fig. 2(f) shows that only 1.12% of the measured data points have a ratio higher than 0.6. This low proportion of oxidation sites indicates that our method induces minimal oxidation of BP, significantly lower than that reported in previous methods (Table S2).

2.3　Photoelectric properties of the BP ink film photodetector

We further investigated the broadband optoelectronic detection capability of BP ink film optoelectronic devices. The schematic diagram of BP ink photodetector,

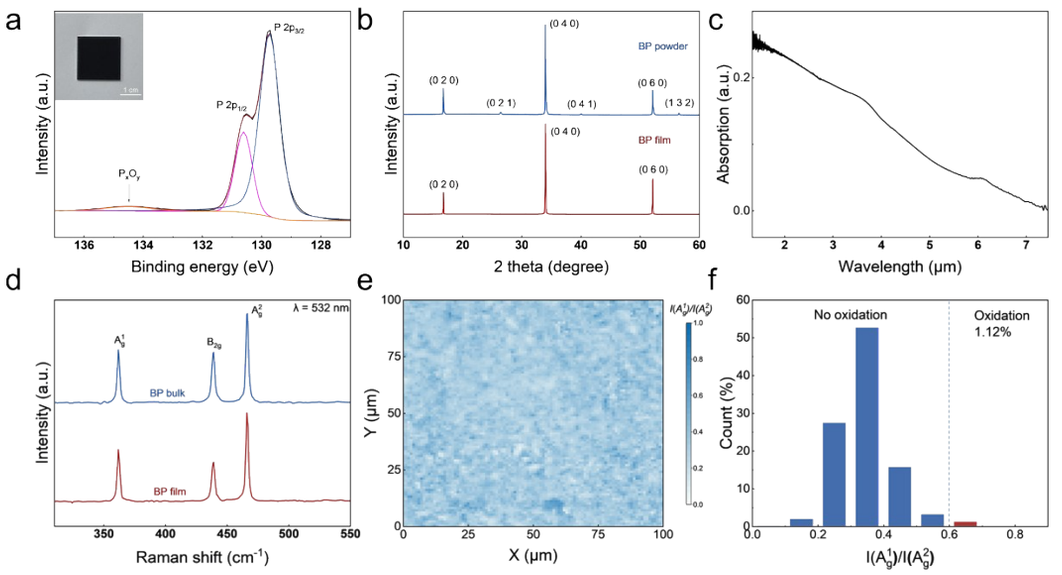

Fig. 2 Characterization of uniformity and oxidation degree of large-area BP ink film: (a) High-resolution X-ray photoelectron spectroscopy (XPS) results of the P 2p signal for the BP film, the inset shows a BP thin film formed on a silicon substrate via spin-coating of BP ink; (b) X-ray diffraction (XRD) data of BP film on silicon substrate and BP source powder; (c) The absorption spectrum (a. u.) obtained from transflection-mode FTIR spectroscopy of the BP film spanning 1. 33 μm to 7. 45 μm; (d) Raman spectrum for BP film and BP bulk; (e) Raman map of the intensity ratio, $I(A_g^1)/I(A_g^2)$, with 1-μm spatial step on a ~100 μm - by - 100 μm area of BP film; (f) Corresponding histogram of the map in e. Spectra with intensity ratios below 0. 6 provide evidence of oxidation at those locations

图2 大面积黑磷油墨薄膜的均匀性与氧化程度表征:(a) 黑磷薄膜P 2p信号的高分辨率X射线光电子能谱结果,插图为通过旋涂黑磷油墨在硅基底上形成的黑磷薄膜示意图;(b) 硅基底上黑磷薄膜与黑磷源粉末的X射线衍射数据对比;(c) 在1. 33 μm至7. 45 μm波长范围内,通过透反射模式傅里叶变换红外光谱获得的黑磷薄膜吸收光谱(任意单位);(d) 黑磷薄膜与黑磷块体材料的拉曼光谱对比;(e) 在约100 μm × 100 μm的黑磷薄膜区域上,以1 μm空间步进扫描得到的拉曼强度比$I(A_g^1)/I(A_g^2)$的二维映射图;(f) 图(e)中映射图对应的强度比分布直方图,强度比值低于0. 6的光谱为该位置存在氧化的证据

prepared with an 850 nm thick BP ink film, is presented in Fig. 3(a). The detailed device fabrication process is outlined in Method. A cross-sectional SEM image of the device can be found in Fig. S6. The optical microscope photograph of the device is illustrated in Fig. S7, where the pixel area is a rectangle measuring 35 μm in length and 5 μm in width. Fig. 3(b) displays the *I*–*V* characteristic curves under dark conditions and 1060 nm laser irradiation. Under laser illumination, BP devices demonstrate significant photoconductive effects. At a bias voltage of +0. 5 V and a laser power density of 32. 05 W·cm^{-2}, the peak photocurrent reaches 85 nA at a wavelength of 1 060 nm, while the dark current density of the device is only 4. 57 mA/cm^2. Fig. 3(c) shows *I*–*T* response under laser irradiation at different wavelengths maintaining a power density. The photocurrent of BP devices increases with wavelength from 633 nm to 1 550 nm.

To more accurately assess the response performance of the BP ink photodetectors, we conducted variable power tests under laser illumination at 633, 1 550, and 3366 nm. Fig. 3(d) illustrates the relationship between the photocurrent and optical power density. This relationship can be described by the equation: $I_{ph} = P^{\alpha}$, where I_{ph} represents the net photocurrent, calculated by subtracting the dark current (I_{dark}) from the current (I_{light}) under laser irradiation. P denotes the optical power density, and α is the fitting index. Under illumination at 633, 1550, and 3366 nm, the fitting index α is approximately 0. 73. All α values are less than 1, which can be attributed to the complex processes of carrier generation, capture, and recombination[48]. This sublinear behavior indicates the presence of trap states in the channel, contributing to the photoconductive gain of the device.

Responsivity (R) and detectivity (D^*) are key parameters for evaluating the performance of photodetectors. R is defined as:

$$R = \frac{I_{ph}}{P \times A} \quad ,(1)$$

where A is the area of the BP device, A=175 μm^2. Meanwhile, D^* is calculated as:

$$D^* = \sqrt{\frac{A\Delta f}{i_n^{\,2}}}\,R \quad ,(2)$$

where Δf is electrical bandwidth, i_n^2 is noise current density. The noise current of the BP device is presented in Fig. 3(e). As shown in **Fig. 3(f)**, under illumination at different wavelengths, R and D^* of the photodetector

follow the same trend with increasing laser power. The peak R and D^* of the device are 4.52 mA W^{-1} and 1.7×10^8 cm $Hz^{1/2}$ W^{-1} at 1 550 nm, respectively. At high optical power densities, both R and D^* decrease due to the saturation of optical absorption and carrier extraction processes[49]. Response time of BP ink device was characterized in Fig. 3(g). The rise time and decay time are defined as the time required for the photocurrent to increase from 10% to 90% of its maximum value, and to decrease from 90% to 10%, respectively. Under illumination at 633 nm, 1 550 nm, and 3 366 nm, the rise times are approximately 206 μs, 185 μs, and 232 μs, while the decay times are about 156 μs, 150 μs, and 225 μs, respectively.

Figure 3(h) illustrates R of BP ink device under laser irradiation ranging from 633 nm to 1 550 nm, both immediately after fabrication and after 60 days of storage. The trend of R with respect to wavelength aligns with the photoelectric current depicted in Fig. 3(d). R increases with the wavelength within this range. To further validate the exceptional broadband optical response of the BP photodetector, we assessed its MWIR response capabilities using an adjustable mid-wave infrared light source. The test results are presented in Fig. S8. The responsivity was calculated over a wavelength range of 2 217 nm to 3 951 nm. At optical power density of 38.21 mW cm^{-2}, a peak responsivity of 4.67 mA W^{-1} at 2 513 nm in Fig. 3(i). The device retained 75% of its initial responsivity after 60 days. The blue shift in the peak wavelength is attributed to the presence of numerous few-layer BP nanosheets in the ink film, which significantly influence its photoelectric properties. Additionally, the interlayer transitions within the stacked BP nanosheets broaden the device's response range, extending it to 3951 nm. These key performance indicators underscore the feasibility of utilizing spin-coated BP films derived from BP ink to fabricate high-performance photodetectors.

2.4 Coded communication and Mid-infrared snapshot imaging

We demonstrated applications in high-speed optical communication and mid-infrared snapshot imaging. Fig. 4(a) illustrates a complete reflection imaging system, which consists of a laser reflection optical path, a precision scanning platform, and a synchronous signal acquisition module. During the imaging process, the detector converts the reflected light signal into an electrical signal, which is subsequently collected and processed by a computer. By encoding the working state of the laser, BP devices have exhibited excellent optical communication capabilities. The strings "SITP" and "SHU" are converted into binary sequences according to the American Standard Code for Information Interchange (ASCII) to control the operating state of the laser. As shown in Fig. 4(b), when the 1550 nm laser is modulated according to the "SITP" binary sequence, the BP photodetector can quickly and accurately detect the corresponding optical signal. Similarly, when modulating a 1060 nm laser according to the "SHU" sequence, the collected signal is presented in Fig. 4(c).

Furthermore, we have demonstrated the scanning imaging capability of the unit BP ink device across the visible to near-infrared spectrum. The illustration in Fig. 4(d) depicts a custom-designed imaging target, which consists of a high reflectivity metal pattern deposited on a SiO_2/Si substrate. This pattern is defined as the "SITP" letter pattern through electron beam exposure. Under laser irradiation at 633, 1 060, and 1 550 nm, the letter patterns were scanned using the reflective imaging system shown in Fig. 4(a), and the imaging results are displayed in Fig. 4(d)-4(f), respectively. Notably, compared to the imaging effect in the visible range (633 nm), the image captured at 1550 nm exhibits a signal-to-noise ratio (SNR) of up to 33.8, indicating a clearer imaging quality. This high-performance behavior underscores the potential application of thin film devices prepared by spin coating BP ink in high-resolution imaging and infrared coding communication.

Unit photodetectors require physical movement or temporal reuse to scan a scene, whereas arrays can sample multiple points in parallel, achieving data acquisition speeds that far exceed those of point-by-point scanning. Therefore, after evaluating the imaging performance of the unit BP ink photodetector, we employed a large-scale ink film preparation process to deposit a uniform BP ink film onto a thin film transistor (TFT). TFT chip consists of a 64 × 64 transistor array. Given the strong penetration ability of mid-infrared light in materials and the necessity for a thicker absorption layer to enhance light response, we deposited an 850 nm BP film on the surface of the TFT. In contrast to thin-layer BP detectors produced by mechanical exfoliation, TFT-integrated arrays require a thicker BP absorption layer, which is a compromise due to the inherent dark current of the readout system. Subsequently, metal electrodes were thermally evaporated onto the BP ink film, and the deposited metal electrodes were grounded, as illustrated in Fig. S9. A comparative summary of recently reported black phosphorus (BP) and BP heterojunction arrays prepared using different methods is presented in Table S3, including array size, wavelength, R, D*, and response time. The results indicate that the BP array we fabricated exhibits a relatively large array scale and broadband photoresponse, with performance and response time approaching those of mechanically exfoliated BP heterojunction arrays.

During the infrared imaging process, it is essential to orient the TFT chip with BP array devices deposited onto the readout device (with one side of the Cr/Au electrode facing downward and grounded) and connect the readout leads, as depicted in Fig. S9. Note that due to the photoconductive mode of the BP ink film detector, the TFT circuit is required to control the scanning voltage, which to some extent alleviates the crosstalk problem of the device itself. The high transmission of visible to infrared light through the indium tin oxide (ITO) electrode on the back of the TFT enables the BP array detector to detect incident light. The detailed array preparation and testing procedures can be found in Method. It is

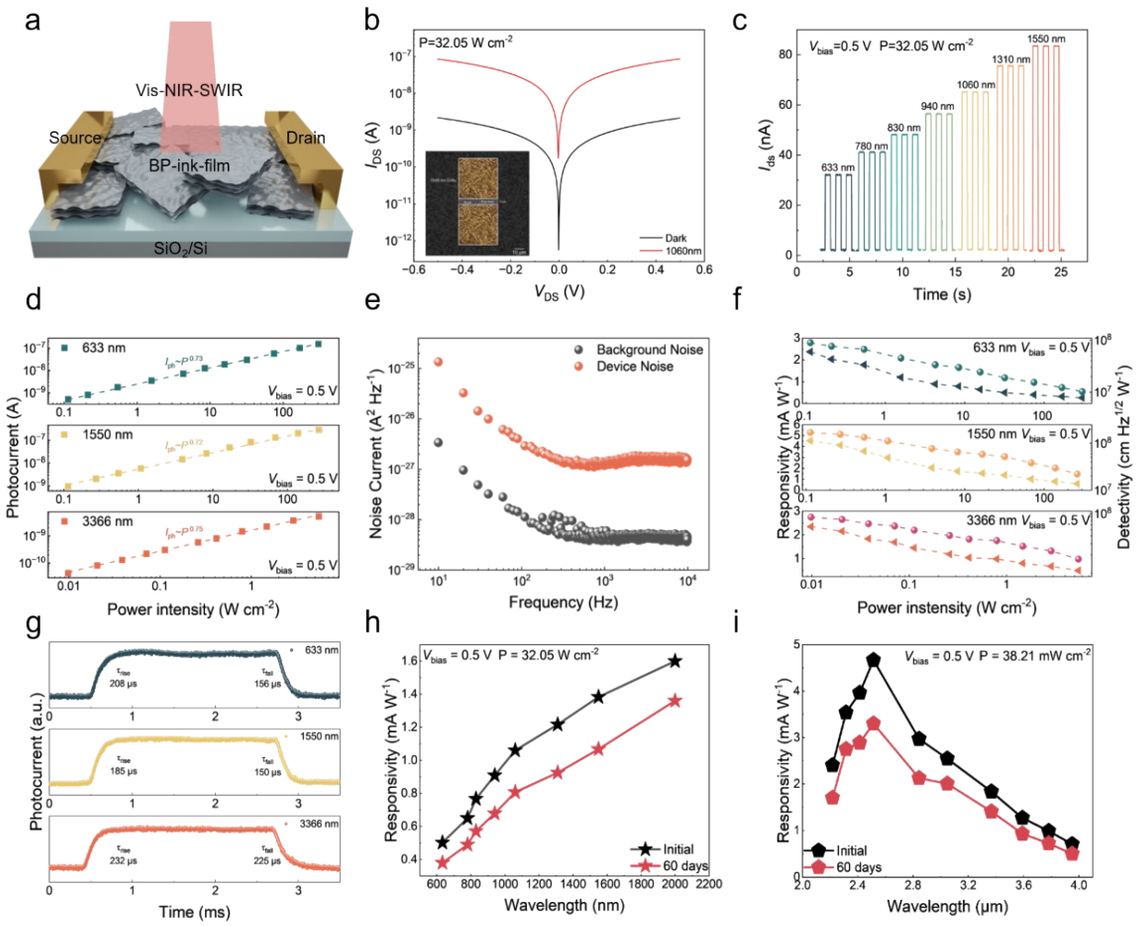

Fig. 3 The room temperature wide spectral range photoelectric characteristics of the photoconductive BP ink thin film photodetector: (a) The schematic diagram of the BP photodetector with a broadband response; (b) *I-V* curves of the BP photodetector in the dark and under the illumination of a 1 060 nm laser; (c) *I-T* curves of the BP photodetector under illumination with different monochromatic lasers; (d) Light power-dependent photocurrent; (e) Noise current spectral density of the BP photodetector at 0. 5 V bias from 10 Hz to 10^4 Hz; (f) Responsivity and specific detectivity; (g) Response time as a function of laser power intensity under illumination at 633 nm, 1 550 nm, and 3 366 nm, respectively; The wavelength-dependent light response of black phosphorus photodetectors in the (h) visible near-infrared and (i) NWIR to MWIR, as well as their response ability after being placed in the atmosphere for 60 days. The black line represents the original response capability, and the red line represents the response capability after being placed for 60 days

图3 光电导型黑磷油墨薄膜光电探测器的室温宽光谱范围光电特性:(a) 具有宽带响应的黑磷光电探测器结构示意图;(b) 黑磷光电探测器在黑暗中和1060 nm激光照射下的电流-电压曲线;(c) 在不同单色激光照射下黑磷光电探测器的电流-时间曲线;(d) 光功率依赖的光电流;(e) 在0. 5 V偏压下,黑磷光电探测器在10 Hz至10^4 Hz频率范围内的噪声电流谱密度;(f) 响应度与比探测率;(g) 响应时间分别作为633 nm、1 550 nm和3 366 nm激光照射下光功率强度的函数;黑磷光电探测器在(h) 可见光-近红外及(i) 近红外-中波红外区域的波长依赖光响应以及大气放置60天后的响应能力。其中黑色线代表原始响应能力,红色线代表放置60天后的响应能力

important to note that the metal electrodes on the back have been grounded, and the actual circuit readout depends on the scanning control program of the TFT system. To characterize the uniformity of the photoelectric response of the array, we analyzed the dark current distribution across all 4 096 pixels, as shown in Fig. 5(b). We have computed the uniformity of electronic devices in BP ink film arrays that have been previously published. The dark current variation among the 4 096 pixels in the BP array does not exceed 10. 16%. Under infrared illumination, storage capacitors collect holes driven by external voltage, and analog-to-digital converters generate the corresponding digital image signals. We calculated the photocurrent distribution of the 4 096 pixels under 3 300 nm infrared light irradiation, revealing a pixel light response non-uniformity of 10. 1%. The uniformity test of the photoelectric response of the BP ink film array is shown in Fig. 5(c). The statistical histogram of array pixels is shown in Fig. 5(d). This indicates that the gradient centrifugation strategy and the BP ink film prepared

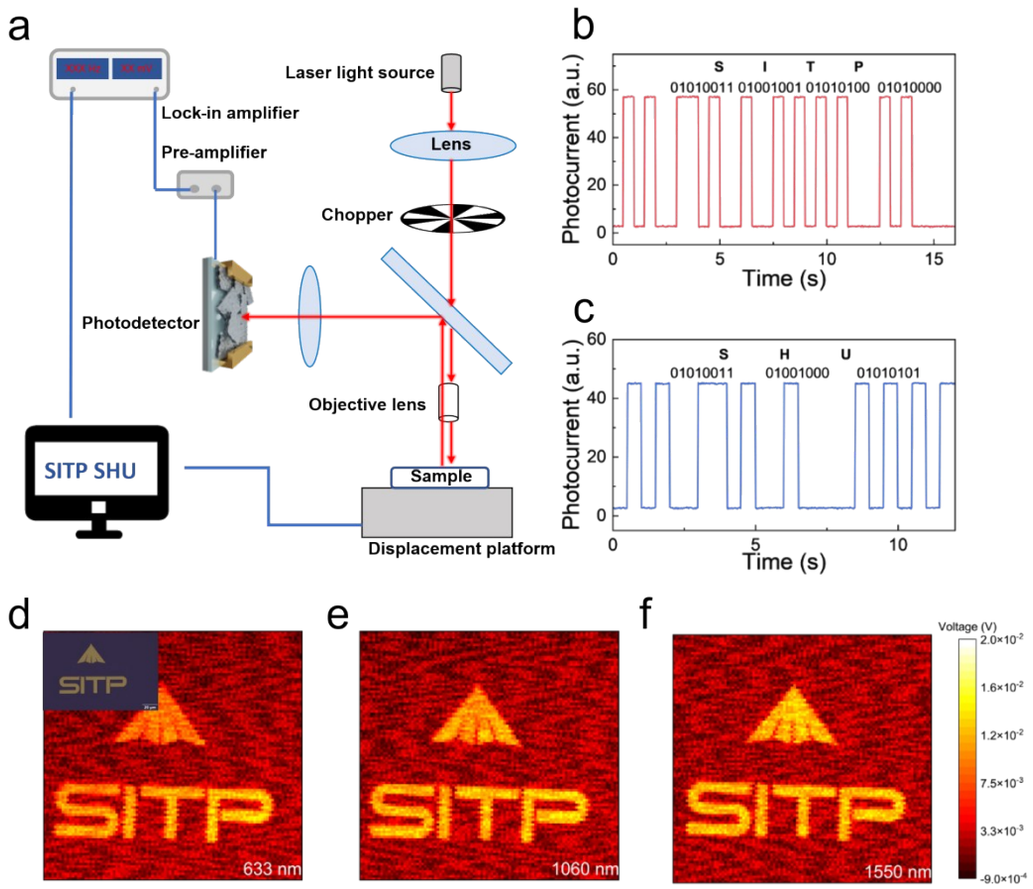

Fig. 4　Coded communication and broadband imaging demonstration based on BP ink thin film photodetector: (a) A schematic illustration of the reflection imaging system; (b, c) *I-T* characteristics of the BP photodetector used for high-speed optical communication; (d, e, f) High-resolution imaging patterns of "SITP" under 633 nm, 1 060 nm, and 1 550 nm laser illumination, respectively. Inset in (d): Optical microscope image of the target sample used for imaging

图4　基于黑磷油墨薄膜光电探测器的编码通信与宽带成像演示:(a) 反射式成像系统的结构示意图;(b, c) 用于高速光通信的黑磷光电探测器的电流-时间特性曲线;(d, e, f) 分别在633 nm、1 060 nm和1 550 nm激光照射下获得的高分辨率"SITP"成像图案。图(d)中的插图:用于成像的目标样品的光学显微镜图像

using low boiling point solvents are advantageous.

To demonstrate the real-time infrared imaging capability, a transparent plastic film was placed over the array surface, and the abbreviation "SH" for Shanghai was handwritten on it with a marker. Under illumination by a 3 300 nm infrared light source, the TFT readout system was used for synchronized imaging. Imaging results taken at 3-second intervals are presented in Fig. 5(e). The clear contours indicate minimal photoelectric crosstalk between adjacent pixels, illustrating the potential application of BP ink thin film optoelectronic arrays.

3　Conclusions

We reported a mid-wavelength infrared photodetector array based on BP ink film, and demonstrated it through uncooled infrared snapshot imaging. The 4 096-pixel infrared photoelectric array has achieved several key performance indicators at room temperature: an average detectivity (D*) of up to 1.7×10^8 cm $Hz^{1/2}W^{-1}$, wavelength range of 0.6 - 4 μm, and a response time of 206 μs. The dark current non-uniformity of the array is as low as 10.16%, with a response non-uniformity of 10.1%. The significant performances can be attributed to improvements in the preparation process of ink optoelectronic devices. The gradient centrifugation strategy has refined the traditional ink preparation process, yielding BP nanosheets with a concentrated particle size and thickness distribution. Additionally, employing low boiling point solvents, such as ethanol, to lower the processing temperature of the ink film to room temperature significantly mitigated performance degradation caused by the spontaneous oxidation of BP nanosheets. This high-quality ink preparation method undoubtedly paves the way for the development of large-area optoelectronic chips and represents a substantial advancement in the next generation of room temperature, high-performance, and CMOS-

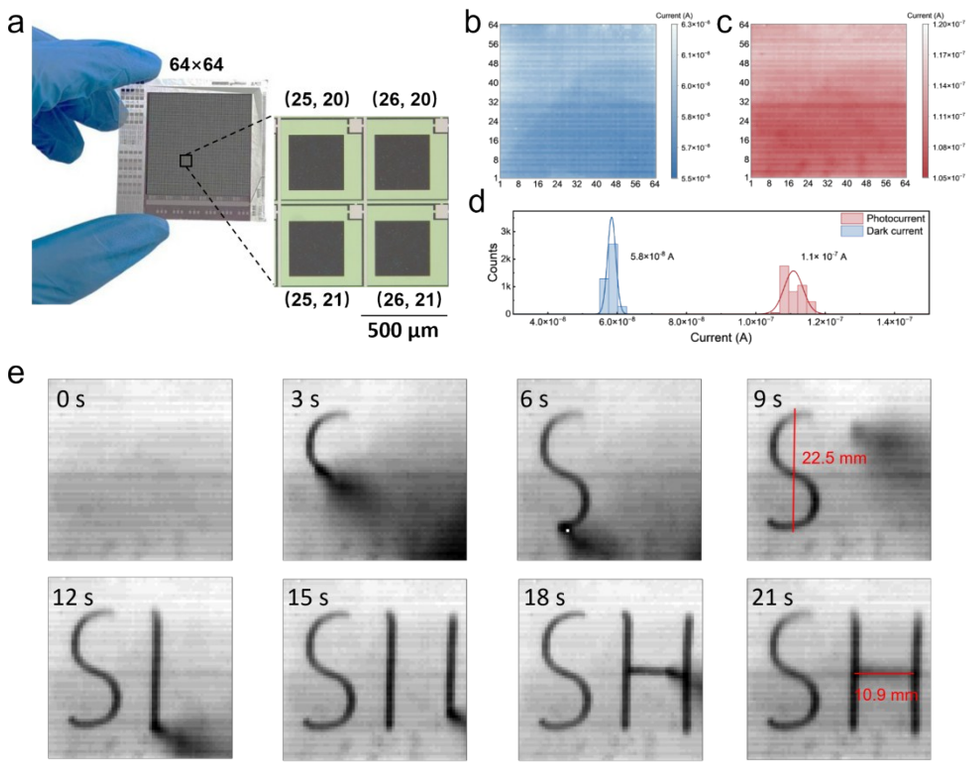

Fig. 5 Mid-infrared snapshot imaging based on high uniformity BP ink film photodetector array: (a) photograph of the 64 × 64 MWIR TFT imaging array backplane based on black phosphorus ink (inset: optical microscope image of the pixel area); (b) dark current distribution of BP imaging array; (c) photocurrent distribution of the BP imaging array; (d) statistical histogram of dark current and photoelectric response of array pixels; (e) imaging results of the handwritten letters "S" and "H", represented by the photocurrent measured at each pixel

图5 基于高均匀性黑磷油墨薄膜光电探测器阵列的中波红外快照成像:(a) 基于黑磷油墨的64×64中波红外薄膜晶体管成像阵列背板照片(插图:像素区域的光学显微镜图像);(b) 黑磷成像阵列的暗电流分布;(c) 黑磷成像阵列的光电流分布;(d) 阵列像素的暗电流与光响应统计直方图;(e) 以各像素点测得的光电流表示的手写字母"S"和"H"的成像结果.

compatible mid-infrared optoelectronic imaging technology.

Supporting Information

The supporting Information is available free of Complete schematic diagram of the BP ink film preparation process. (Figure S1); Supernatant photographs and UV - VIS - NIR absorption spectra of BP dispersions. (Figure S2); XPS test results of BP nanosheet with different degrees of oxidation. (Figure S3); TEM and XRD analysis images of BP nanosheets. (Figure S4); Infrared transmission spectroscopy of BP ink film. (Figure S5); Characterization of thickness and morphology of BP ink film. (Figure S6); Optical microscope image of BP ink film photodetector. (Figure S7); IT testing of BP ink film photodetector in the range of 2 217nm to 3 951nm. (Figure S8); Schematic structure of a 64 × 64 MWIR imaging array based on black phosphorus ink. (Figure S9); Processing parameters under ultrasonic treatment time and centrifugal conditions. (Table S1); Comparison Table of BP Ink Preparation Processes. (Table S2); Summary of main indicators of BP photodetector array. (Table S3).

References

[1] Wang Y, Gu Y, Cui A, et al. Fast Uncooled Mid-Wavelength Infrared Photodetectors with Heterostructures of van der Waals on Epitaxial HgCdTe [J]. Advanced Materials, 2022, 34(6): 2107772.
[2] Ou K, Yu F, Li G, et al. Broadband Achromatic Metalens in Mid-Wavelength Infrared [J]. Laser & Photonics Reviews, 2021, 15(9): 2100020.
[3] Zou K, Pang K, Song H, et al. High-capacity free-space optical communications using wavelength- and mode-division-multiplexing in the mid-infrared region [J]. Nature Communications, 2022, 13(1): 7662.
[4] Chen D, March S D, Jones A H, et al. Photon-trapping-enhanced avalanche photodiodes for mid-infrared applications [J]. Nature Photonics, 2023, 17(7): 594-600.
[5] Zorin I, Gattinger P, Ebner A, et al. Advances in mid-infrared spectroscopy enabled by supercontinuum laser sources Development and evaluation of MWIR imaging spectrometer for multi-dimensional detection [J]. Optics Express, 2022, 30(4): 5222-5254.
[6] Yuan L, Wen M, Wang Y, et al. Development and evaluation of MWIR imaging spectrometer for multi-dimensional detection [J]. In-

frared Physics & Technology, 2024, 137: 105148.
[7] Wang Y, Huang K, Fang J, et al. Mid-infrared single-pixel imaging at the single-photon level [J]. Nature Communications, 2023, 14 (1): 1073.
[8] Zhao Y, Kusama S, Furutani Y, et al. High-speed scanless entire bandwidth mid-infrared chemical imaging [J]. Nature Communications, 2023, 14(1): 3929.
[9] Ma H, Huang K, Fang J, et al. Mid-infrared single-pixel imaging via two-photon optical encoding [J]. PhotoniX, 2025, 6(1): 34.
[10] Li L, Liu H, Li Y, et al. Integrative proteomic characterization of trace FFPE samples in early-stage gastrointestinal cancer [J]. Proteome Science, 2022, 20(1): 5.
[11] Dam J S, Tidemand-Lichtenberg P, Pedersen C. Room-temperature mid-infrared single-photon spectral imaging [J]. Nature Photonics, 2012, 6(11): 788-793.
[12] Martin M, Chong A, Biljecki F, et al. Infrared thermography in the built environment: A multi-scale review [J]. Renewable and Sustainable Energy Reviews, 2022, 165: 112540.
[13] Tratt D M, Young S J, Hackwell J A, et al. MAHI: An Airborne Mid-Infrared Imaging Spectrometer for Industrial Emissions Monitoring [J]. IEEE Transactions on Geoscience and Remote Sensing, 2017, 55(8): 4558-4566.
[14] Liu T, Li Y F, Liu H, et al. RISIR: Rapid Infrared Spectral Imaging Restoration Model for Industrial Material Detection in Intelligent Video Systems [J]. IEEE Transactions on Industrial Informatics, 2019, 10.1109/TII.2019.2930463: 1-1.
[15] Sharif S S, Banad Y M. Revolutionizing Infrared Detection in Defense Applications: A Nanophotonic Approach Leveraging 2D Materials for Enhanced Mid-IR Absorption [J]. 2024 IEEE Research and Applications of Photonics in Defense Conference (RAPID), 2024, 10.1109/RAPID60772.2024.10646969: 1-2.
[16] Wang K, Zhao L, Li K, et al. Development of tunable mid-infrared laser at 10 - 25 μm [J]. Microwave And Optical Technology Letters, 2024, 66(8): e34299.
[17] Jia B W, Tan K H, Loke W K, et al. Monolithic Integration of InSb Photodetector on Silicon for Mid-Infrared Silicon Photonics [J]. ACS Photonics, 2018, 5(4): 1512-1520.
[18] Wang S Y, Wang Q, Luo H, et al. InSb all-dielectric metasurface for ultrahigh efficient Si-based mid-infrared detection [J]. Optics Letters, 2024, 49(10): 2641-2644.
[19] Chen X, Wang M, Zhu L, et al. Mid-infrared modulated photoluminescence mapping to investigate in-plane distributions of bandedge transitions in As-doped HgCdTe [J]. Applied Physics Letters, 2023, 123(15): 151105.
[20] Zhang Y, Fu Z, Fu Q, et al. Mid-wave infrared multispectral imaging with HgCdTe photodetector Type-II Superlattice Mid-Wavelength Infrared Focal Plane Arrays for CubeSat Hyperspectral Imaging [J]. Optics Express, 2025, 33(13): 27026-27032.
[21] Hu W, Ye Z, Liao L, et al. 128 × 128 long-wavelength/mid-wavelength two-color HgCdTe infrared focal plane array detector with ultralow spectral cross talk [J]. Optics Letters, 2014, 39(17): 5184-5187.
[22] Hu W D, Chen X S, Ye Z H, et al. A hybrid surface passivation on HgCdTe long wave infrared detector with in-situ CdTe deposition and high-density hydrogen plasma modification [J]. Applied Physics Letters, 2011, 99(9): 091101.
[23] Ting D Z, Rafol S B, Khoshakhlagh A, et al. Type-II Superlattice Mid-Wavelength Infrared Focal Plane Arrays for CubeSat Hyperspectral Imaging [J]. IEEE Photonics Technology Letters, 2022, 34(6): 329-332.
[24] Kwan D, Kesaria M, Anyebe E A, et al. Recent trends in 8 - 14 μm type-II superlattice infrared detectors [J]. Infrared Physics & Technology, 2021, 116: 103756.
[25] Liu Y, Huang Y, Duan X. Van der Waals integration before and beyond two-dimensional materials [J]. Nature, 2019, 567(7748): 323-333.
[26] Hu S, Ye J, Liu R, et al. Valley dynamics of different excitonic states in monolayer WSe2 grown by molecular beam epitaxy [J]. Journal of Semiconductors, 2022, 43(8): 082001.
[27] Bansal S, Jain A, Kumar S, et al. Optoelectronic performance prediction of HgCdTe homojunction photodetector in long wave infrared spectral region using traditional simulations and machine learning models [J]. Scientific Reports, 2024, 14(1): 28230.
[28] Dai M, Zhang X, Hu Y, et al. Vertical Black Phosphorus Photodiodes with High Quantum Efficiency for Mid-Infrared Detection at Room Temperature [J]. Advanced Functional Materials, 2025, 35 (29): 2501467.
[29] Chen X, Lu X, Deng B, et al. Widely tunable black phosphorus mid-infrared photodetector [J]. Nature Communications, 2017, 8 (1): 1672.
[30] Bullock J, Amani M, Cho J, et al. Polarization-resolved black phosphorus/molybdenum disulfide mid-wave infrared photodiodes with high detectivity at room temperature [J]. Nature Photonics, 2018, 12 (10): 601-607.
[31] Liang J, Hu Y, Ding L, et al. 2D black arsenic phosphorous [J]. Journal of Semiconductors, 2024, 45(3): 030201.
[32] Xu T, Zhong F, Wang P, et al. Van der Waals mid-wavelength infrared detector linear array for room temperature passive imaging [J]. Science Advances, 2025, 10(31): eadn0560.
[33] Corletto A, Myagmarsereejid P, Wang S, et al. Scalable Fabrication of Black Phosphorous Films for Infrared Photodetector Arrays [J]. Advanced Science, 2024, 11(35): 2403182.
[34] Jeon Y, Rhee D, Wu B, et al. Electrochemically exfoliated phosphorene nanosheet thin films for wafer-scale near-infrared phototransistor array [J]. npj 2D Materials And Applications, 2022, 6(1): 82.
[35] Wijaya T J, Higashitarumizu N, Wang S, et al. Mechanically flexible mid-wave infrared imagers using black phosphorus ink films [J]. Nature Communications, 2025, 16(1): 5972.
[36] Gupta N, Wang S, Higashitarumizu N, et al. Large-scale efficient mid-wave infrared optoelectronics based on black phosphorus ink [J]. Science Advances, 2023, 9(49): eadi9384.
[37] Hanlon D, Backes C, Doherty E, et al. Liquid exfoliation of solvent-stabilized few-layer black phosphorus for applications beyond electronics [J]. Nature Communications, 2015, 6(1): 8563.
[38] Kim J I, Higashitarumizu N, Wang S, et al. Multicolor Inks of Black Phosphorus for Midwave-Infrared Optoelectronics [J]. Advanced Materials, 2024, 36(30): 2402922.
[39] Coleman J N, Lotya M, O'Neill A, et al. Two-Dimensional Nanosheets Produced by Liquid Exfoliation of Layered Materials [J]. Science, 2011, 331(6017): 568-571.
[40] Jun H Y, Ryu S O, Kim S H, et al. Inkjet Printing of Few-Layer Enriched Black Phosphorus Nanosheets for Electronic Devices [J]. Advanced Electronic Materials, 2021, 7(10): 2100577.
[41] Mourdikoudis S, Liz-Marzán L M. Oleylamine in Nanoparticle Synthesis [J]. Chemistry of Materials, 2013, 25(9): 1465-1476.
[42] Xiao H, Zhao M, Zhang J, et al. Electrochemical cathode exfoliation of bulky black phosphorus into few-layer phosphorene nanosheets [J]. Electrochemistry Communications, 2018, 89: 10-13.
[43] Lee K, Higashitarumizu N, Wang S, et al. Meter-scale van der Waals films manufactured via one-step roll printing [J]. Science Advances, 2024, 10(36): eadq0655.
[44] Woomer A H, Farnsworth T W, Hu J, et al. Phosphorene: Synthesis, Scale-Up, and Quantitative Optical Spectroscopy [J]. ACS Nano, 2015, 9(9): 8869-8884.
[45] Guo Z, Zhang H, Lu S, et al. From Black Phosphorus to Phosphorene: Basic Solvent Exfoliation, Evolution of Raman Scattering, and Applications to Ultrafast Photonics [J]. Advanced Functional Materials, 2015, 25(45): 6996-7002.
[46] Yasaei P, Kumar B, Foroozan T, et al. High-Quality Black Phosphorus Atomic Layers by Liquid-Phase Exfoliation [J]. Advanced Materials, 2015, 27(11): 1887-1892.
[47] Hu G, Albrow-Owen T, Jin X, et al. Black phosphorus ink formulation for inkjet printing of optoelectronics and photonics [J]. Nature Communications, 2017, 8(1): 278.
[48] Fang H, Hu W. Photogating in Low Dimensional Photodetectors [J]. Advanced Science, 2017, 4(12): 1700323.
[49] Wang F, Liu Z, Zhang T, et al. Fully Depleted Self-Aligned Heterosandwiched Van Der Waals Photodetectors [J]. Advanced Materials, 2022, 34(39): 2203283.